Supplementary Information (SI) for Journal of Materials Chemistry A.
This journal is © The Royal Society of Chemistry 2025

Supporting information

Assemble an Actinide-uranium single atom catalyst on defective MXenes for efficient NO electroreduction

Bin Huang[1], Yifan Wu[2], Zhongyong Zhang[3], Rong Chen[1], Guangyuan Ren[1], Naigen Zhou[2], Neng Li[3]*, Yong Qian[1]*

[1]School of Chemistry and Materials Science, East China University of Technology, Nanchang 330013, Jiangxi, China

[2]School of Physics and Materials Science, Nanchang University, Nanchang 330031, Jiangxi, China

[3]State Key Laboratory of Silicate Materials for Architectures, Wuhan University of Technology, Hubei, 430070, China

*Corresponding author, E-mail: lineng@whut.edu.cn; yqianecit@163.com

Calculation method supplement

The constant-potential method model was used by CP-VASP code [1, 2]. In CP-VASP, E_F (Fermi level) is fixed:

$$\mu_e = \mu_{SHE} + |e|U_{SHE} \quad \text{(S-1)}$$

where μ_e is the electron energy, μ_{SHE} is the work function (-4.6 eV) of the standard hydrogen electrode (SHE) in VASPsol [3]. U_{SHE} is the applied potential vs SHE. The Debye screening length was adjusted to 3.04 Å, representing the compensatory charge [4]. The energy varies with the electrode potential follow a quadratic function as：

$$E(U_{SHE}) = \frac{1}{2}C(U_{SHE} - U_{PZC})^2 + E_{PZC} \quad \text{(S-2)}$$

where C is the capacitance of the system, U_{PZC} is the potential of zero charges, and E_{PZC} is the energy at the zero charges. and. Upon changing the pH value, the electrode potential under the SHE will change to a fixed potential of reversible hydrogen electrode (RHE) as

$$U_{RHE} = U_{SHE} + 0.059 \times pH \quad \text{(S-3)}$$

The *NH_2OH formation step was determined the rate-determining step in our calculations. Thus, the current density associated with this step was calculated, which represent the reactivity of the NO electroreduction reaction. The calculated equations as follows

$$j_{*NH_2O} = 2\frac{F}{N_A} \times \frac{k_b T}{h} \exp(-\Delta G_{*NH_2O} / k_b T) \quad \text{(S-4)}$$

where F is the Faraday constant, N_A is the Avogadro constant, k_b is Boltzmann's constant, and h is Planck constant [5].

Table S1. The E_{f1} (eV) and E_{f2} (eV) were O vacancy of formation energy on six MXenes surface, which obtained from direct and H_2-assisted thermal treatment, respectively.

	Ti_2CO_2-O_v	V_2CO_2-O_v	Cr_2CO_2-O_v	Zr_2CO_2-O_v	Nb_2CO_2-O_v	Mo_2CO_2-O_v
E_{f1}	4.83	3.95	3.89	5.11	4.58	4.26
E_{f2}	1.74	0.86	0.80	2.02	1.49	1.17

The O vacancy of formation energy on MXene surface by direct thermal treatment was calculated as:

$$E_{fl} = E_{ov} + 1/2\ E_{O2} - E_p, \quad \text{(s-5)}$$

where E_{oV}, E_{O2} and E_P are the total energies of the MXenes with an O vacancy, the O_2 molecules in the triplet state, and MXenes, respectively.

The O vacancy of formation energy on MXene surface by H_2-assisted thermal treatment was evaluated as following the reactions:

$$M_2CO_2 + H_2 \rightarrow M_2CO\text{-}1O_v + H_2O \quad \text{(s-6)}$$

where the energies of H_2O and H_2 molecules are used, and the other two terms represent the total energies of the MXenes and MXenes with an O vacancy, respectively.

Table S2. The calculated binding energies of UO_2@MXene between UO_2 and MXenes with O vacancy.

	U@Ti	U@V	U@Cr	U@Zr	U@Nb	U@Mo
E_b (eV)	4.71	3.96	4.03	5.19	4.72	4.15

The binding energies of UO_2@MXene between UO_2 and MXenes with O vacancy were calculated as follows:

$$E_b = E_{ov} + E_{UO2} - E_{total} \quad \text{(s-7)}$$

where E_{oV}, EU_{O2} and E_{total} are the energies of the MXenes with an O vacancy, the UO_2 state, and UO_2@MXenes, respectively.

Table S3. The free energy change (eV) of other key reaction toward NH_3 synthesis on UO_2@MXenes.

Reaction steps	U@Ti	U@V	U@Cr	U@Zr	U@Nb	U@Mo
NO → NOH	0.86	0.19	0.36	1.17	0.39	0.38
NOH → N	-1.83	-0.52	-0.49	-1.67	-1.88	-1.17
NHO → NHOH	-0.37	0.64	0.23	-0.04	0.31	0.59
NHOH → NH_2OH	-0.34	-1.38	-0.76	-0.15	-1.23	-1.49
N → NH	0.37	-0.97	-0.77	0.27	0.08	-0.62
NHOH → NH	-0.26	-1.34	-0.98	-0.80	-1.28	-1.84
NH → NH_2	-2.37	-0.39	-0.63	-0.72	-1.07	-0.39

Table S4. Comparison of various SACs for NO conversion to NH_3

catalysts	U (limiting potential, V)	Suppressing HER
UO_2@Nb_2CO_2 (this work)	−0.14	Yes
Fe-SACs@graphene[6]	−0.26	Yes
Zr@C_2N[7]	−0.33	Yes
2P@C_2N[8]	0	Yes
Cu@h-BN[9]	−0.23	Yes
IrN_3/BP[10]	−0.06	Yes
La@MoS_v[11]	−0.15	Yes
Cu@$Ti_3C_2O_2$-V_0[12]	0	Yes

The $U_{limiting}$ = 0 indicate a spontaneous occurrence of ENOR.

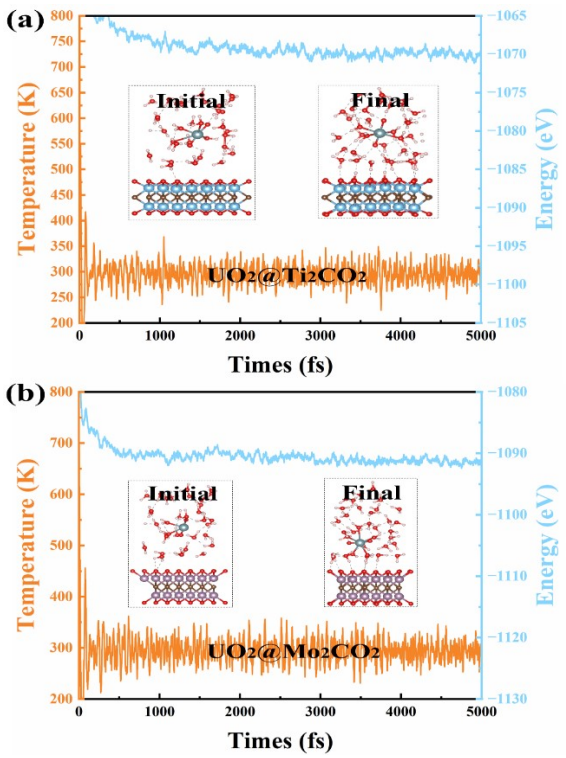

Figure S1. Dynamic evolution when uranyl adsorbate inserts water layer (a) Ti_2CO_2 and (b) Mo_2CO_2 MXenes structures with O vacancy after 5ps AIMD simulation at 298 K.

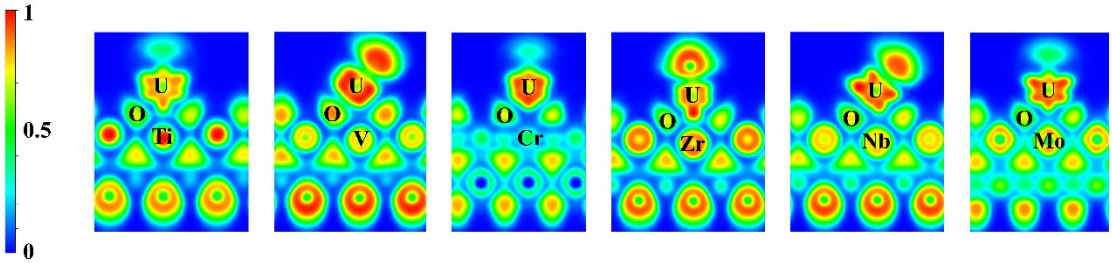

Figure S2. The calculated electron localization function (ELF) for $UO_2@M_2CO_2$, M = Ti, V, Cr, Zr, Nb and Mo, respectively.

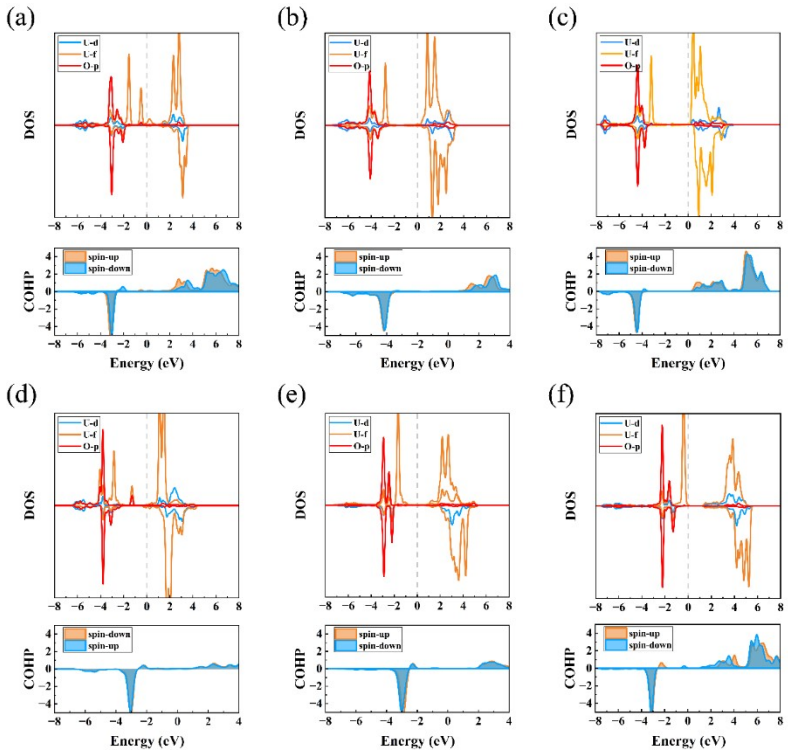

Figure S3. The calculated partial density of states (PDOS) and Crystal Orbital Hamilton Population (COHP) for $UO_2@M_2CO_2$, M = (a) Ti, (b) Zr, (c) V, (d) Nb, (e) Cr and (f) Mo, respectively. The Fermi level was set to the zero.

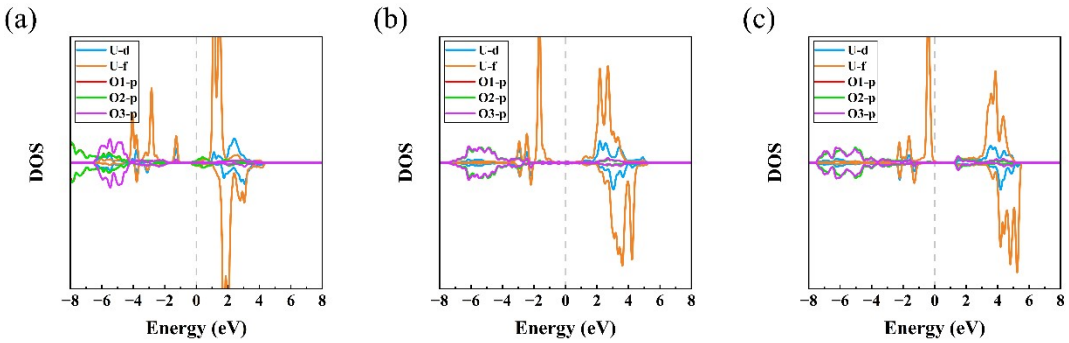

Figure S4. The calculated PDOS of UO_4 moiety for (a) $UO_2@Nb_2CO_2$, (b) $UO_2@Zr_2CO_2$ and (c) $UO_2@Mo_2CO_2$, O1, O2 and O3 represent U connect three oxygen atoms of MXene substrate, respectively. The Fermi level was set to the zero.

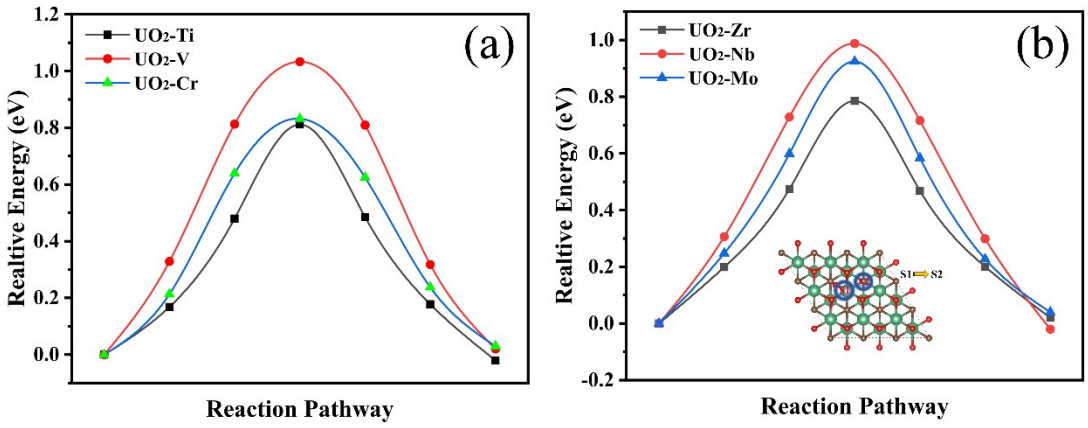

Figure S5. The calculated diffusion barrier of adsorbed UO moiety between S1 and S2 sites for (a) UO_2–Ti, V, Cr, and (b) UO_2–Zr, Nb, Mo.

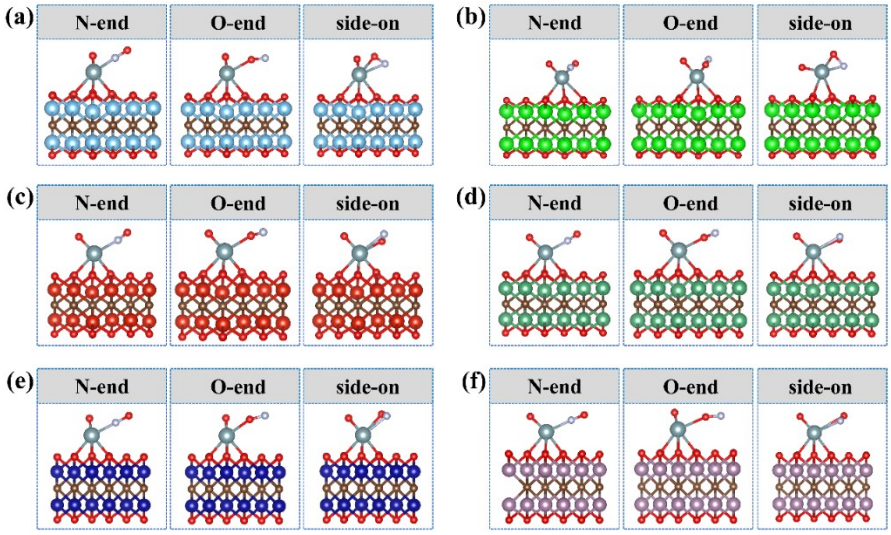

Figure S6. The three modes (N-end, O-end and side end) of adsorbed NO optimized configurations on UO_2@M_2CO_2, M = (a) Ti, (b) Zr, (c) V, (d) Nb, (e) Cr and (f) Mo, respectively.

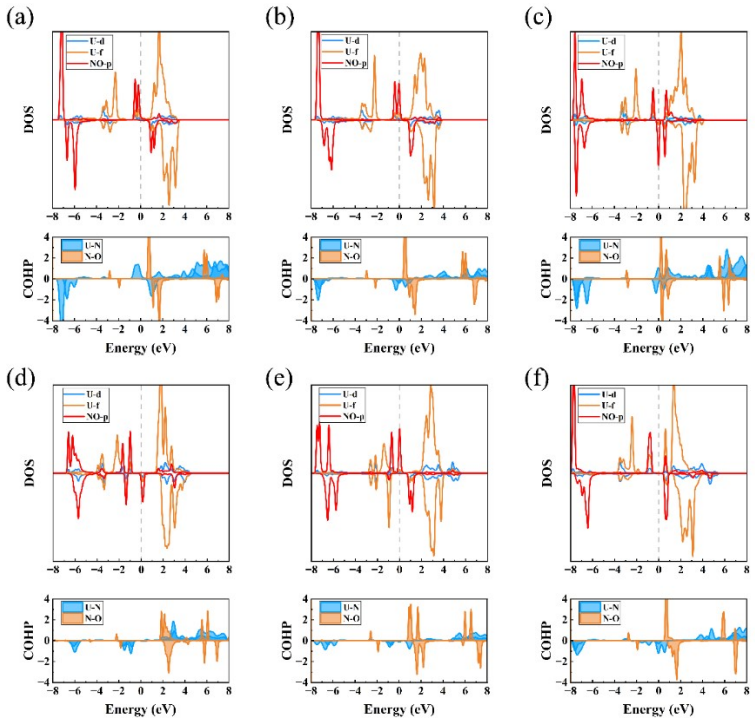

Figure S7. The calculated partial density of states (PDOS) and Crystal Orbital Hamilton Population (COHP) for NO adsorbed on $UO_2@M_2CO_2$, M = (a) Ti, (b) Zr, (c) V, (d) Nb, (e) Cr and (f) Mo, respectively. The Fermi level was set to the zero.

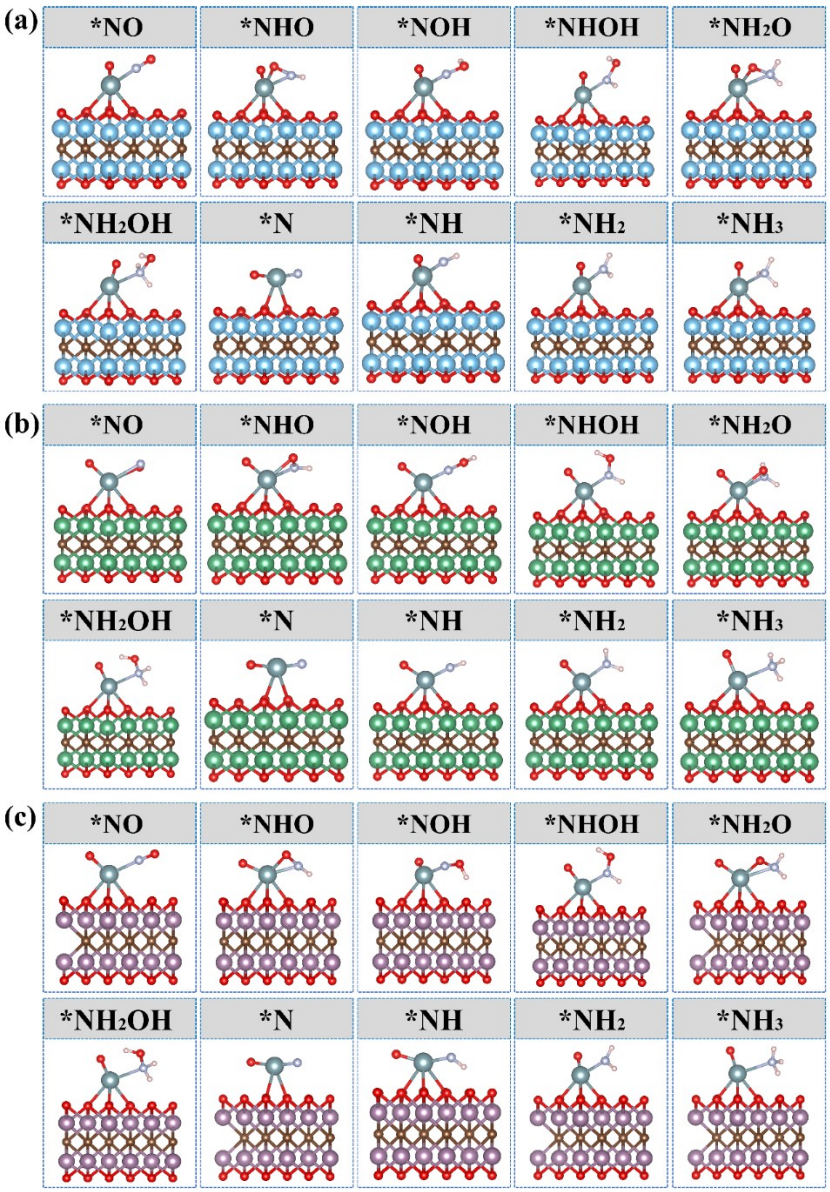

Figure S8. The optimized configurations involved NO conversion to NH_3 pathway on (a) UO_2@Ti_2CO_2, (b) UO_2@Nb_2CO_2 and (c) UO_2@Mo_2CO_2.

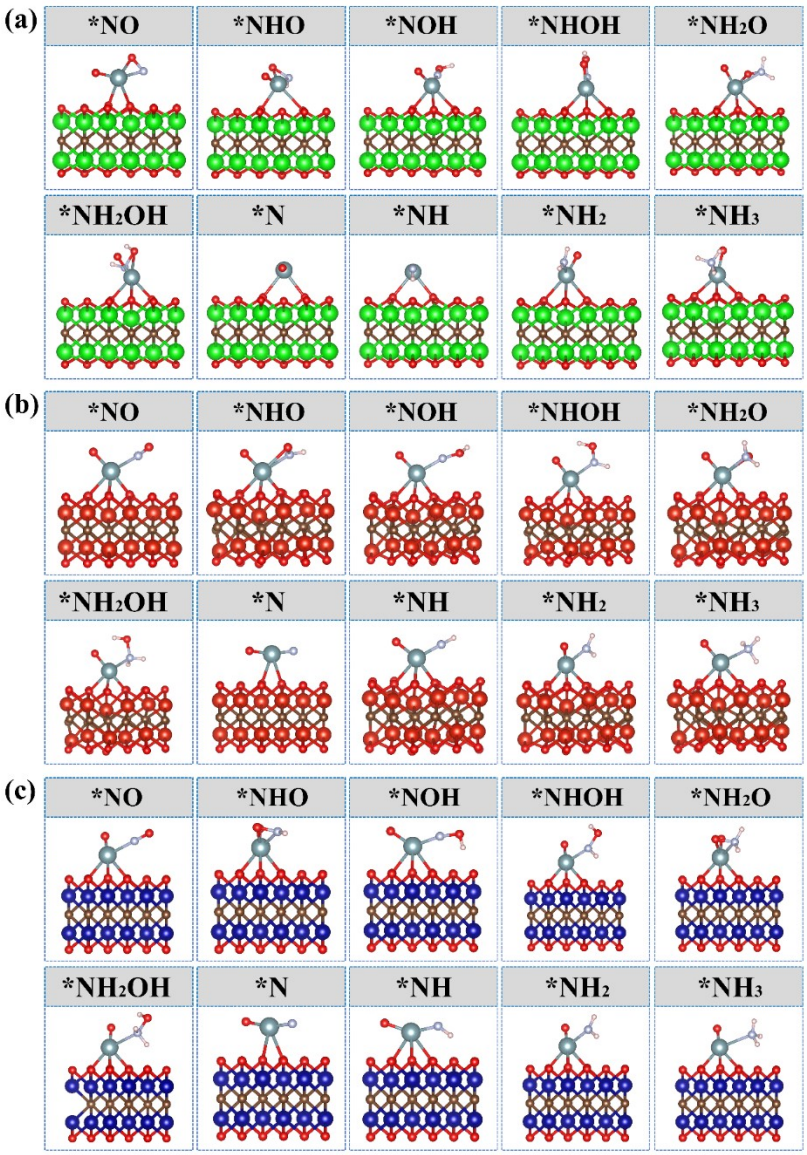

Figure S9. The optimized configurations involved NO conversion to NH_3 pathway on (a) UO_2@Ti_2CO_2, (b) UO_2@Nb_2CO_2 and (c) UO_2@Mo_2CO_2.

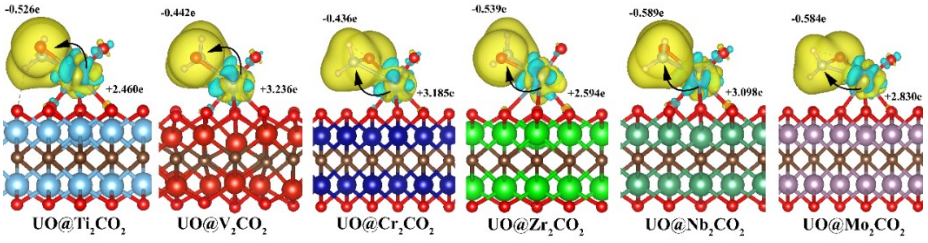

Figure S10. The calculated Bader charge and charge density differences induced by NH_2O adsorption on UO_2@MXenes. Cyan and yellow represent electron charge depletion and accumulation, respectively.

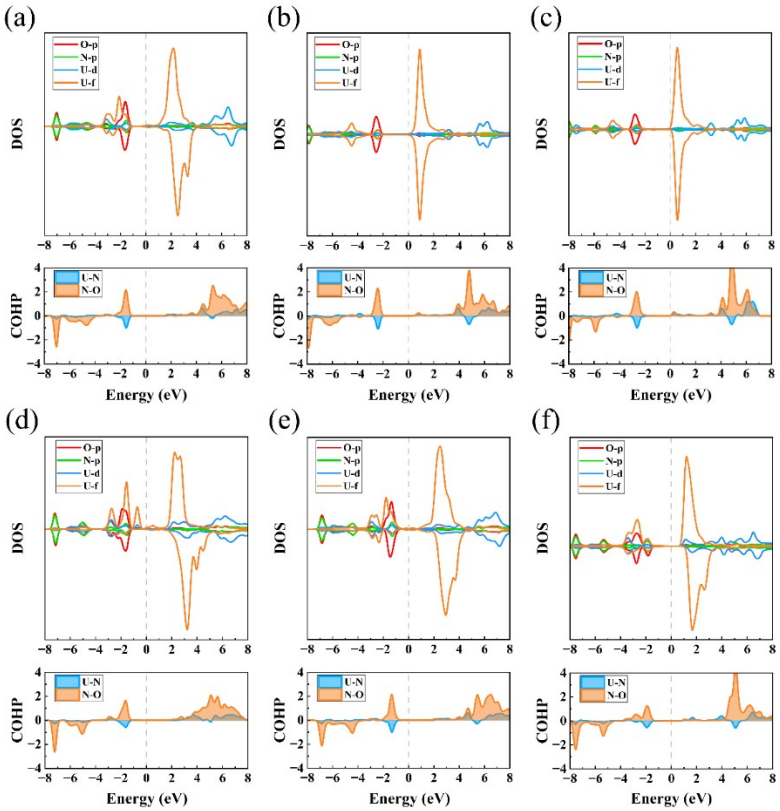

Figure S11. The calculated partial density of states (PDOS) and Crystal Orbital Hamilton Population (COHP) for NH_2O adsorbed on UO_2@M_2CO_2, M = (a) Ti, (b) Zr, (c) V, (d) Nb, (e) Cr and (f) Mo, respectively. The Fermi level was set to the zero.

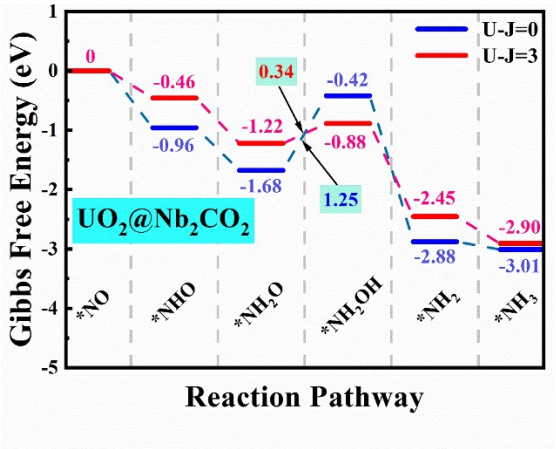

Figure S12. Gibbs free energy distribution diagram of the NO reduction pathway toward NH_3 on UO_2@Nb_2CO_2 catalyst (*U*–*J* value = 0 or 3 eV).

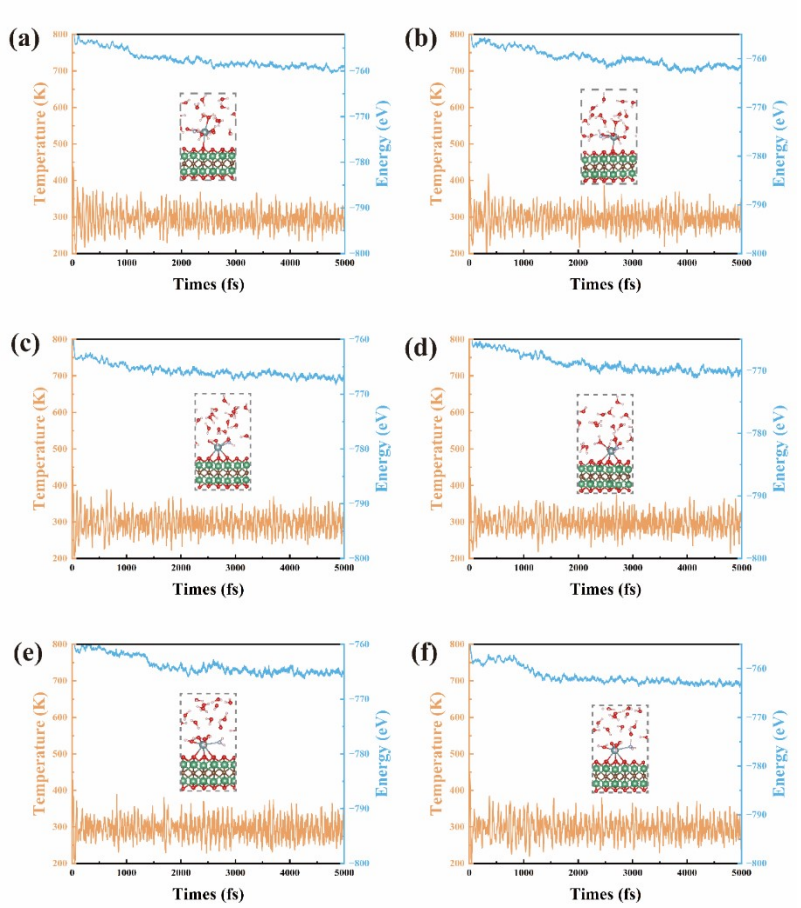

Figure S13. The AIMD results for the (a) NO, (b) NHO, (c) NH_2O, (d) NH_2OH, (e) NH_2 and (f) NH_3 adsorption on UO_2@Nb_2CO_2 by introduction of multiple explicit water layers.

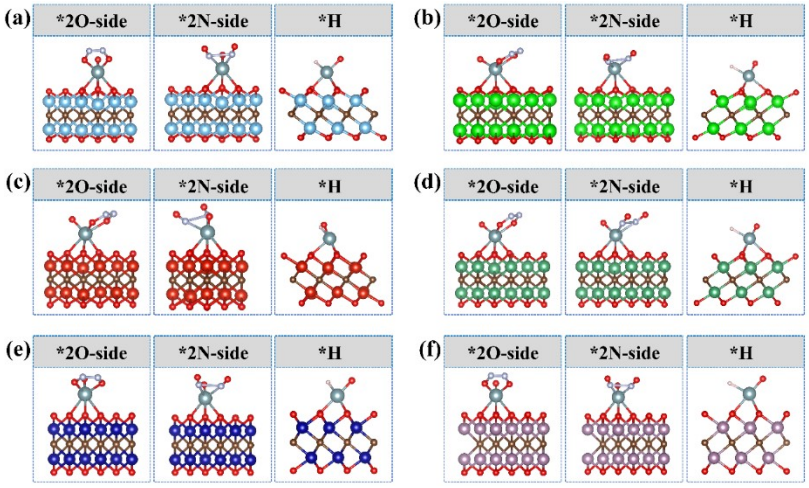

Figure S14. The optimized configurations for *2O-end, *2N-end and *H adsorbed on UO_2@M_2CO_2, M = (a) Ti, (b) Zr, (c) V, (d) Nb, (e) Cr and (f) Mo, respectively.

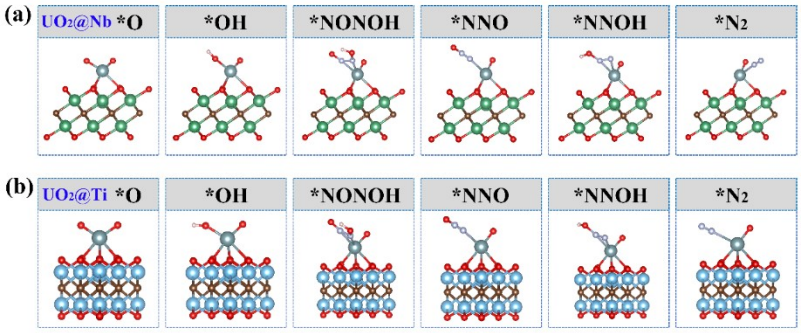

Figure S15. The optimized configurations of competition side reaction toward N_2O and N_2 products on UO_2@Nb_2CO_2 and UO_2@Ti_2CO_2, respectively.

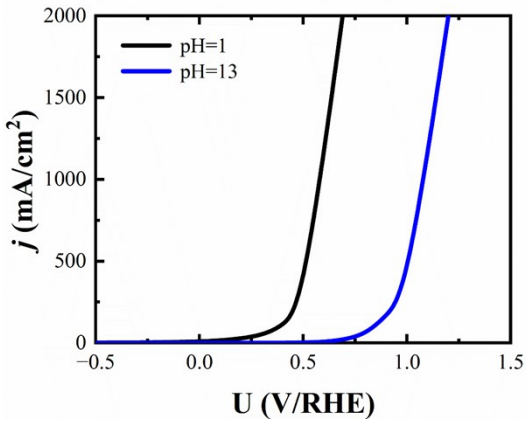

Figure S16. Current density of NO electroreduction reaction as a function of applied potential at pH = 1 (black) and pH = 13 (blue).

References

[1] Zhao, X.; Liu, Y. Origin of Selective Production of Hydrogen Peroxide by Electrochemical Oxygen Reduction. J. Am. Chem. Soc. 2021, 143 (25), 9423−9428.

[2] Yu, S.; Levell, Z.; Jiang, Z.; Zhao, X.; Liu, Y. What Is the Rate-Limiting Step of Oxygen Reduction Reaction on Fe–N–C Catalysts? J. Am. Chem. Soc. 2023, 145 (46), 25352−25356.

[3] Mathew, K.; Sundararaman, R.; Letchworth-Weaver, K.; Arias, T. A.; Hennig, R. G. Implicit solvation model for density-functional study of nanocrystal surfaces and reaction pathways. J. Chem. Phys. 2014, 140, 084106.

[4] Hagopian, A.; Doublet, M.-L.; Filhol, J.-S.; Binninger, T. Advancement of the homogeneous background method for the computational simulation of electrochemical interfaces. J. Chem. Theory Comput. 2022, 18 (3), 1883−1893.

[5] Duan, Z. Y.; Henkelman, G. Calculations of the pH-Dependent Onset Potential for CO Electrooxidation on Au (111). Langmuir 2018, 34, 15268−15275.

[6] Li, H. B.; Wu, D. H.; Wu, J. R.; Lv, W. J.; Duan, Z. Y.; Ma, D. W. Graphene-based iron single-atom catalysts for electrocatalytic nitric oxide reduction: a first-principles study, Nanoscale, 2024, 16, 7058−7067.

[7] Niu, H.; Zhang, Z. F.; Wang, X. T.; Wan, X. H.; Kuai, C. G.; Guo, Y. Z. A Feasible Strategy for Identifying Single-Atom Catalysts Toward Electrochemical NO-to-NH3 Conversion. Small, 2021, 17, 2102396.

[8] Wu, Q.; Wang, H.; Shen, S. Y.; Huang, B. B.; Dai, Y.; Ma, Y. D. Efficient nitric oxide reduction to ammonia on a metal-free electrocatalyst, J. Mater. Chem. A, 2021, 9, 5434−5441.

[9] Sun, P. F.; Wang, W. L.; Zhao, X.; Dang, S. Defective h-BN sheet embedded atomic metals as highly active and selective electrocatalysts for NH_3 fabrication via NO reduction. Phys. Chem. Chem. Phys., 2020, 22, 22627−22634.

[10] Wu, J.; Yu, Y. X. A theoretical descriptor for screening efficient NO reduction electrocatalysts from transition-metal atoms on N-doped BP monolayer, J. Colloid Interface Sci., 2022, 623, 432−444.

[11] He, B. L.; Lv, P.; Wu, D. H.; Li, X.; Zhu, R.; Chu, K.; Ma, D. W.; Jia, Y. Confinement catalysis of a single atomic vacancy assisted by aliovalent ion doping enabled efficient NO electroreduction to NH_3, J. Mater. Chem. A, 2022,10, 18690−18700.

[12] Kong, L. Y.; Wang, M. H.; Wu, C. M. L. From Single Atom to Low-Nuclearity Cluster Immobilized $Ti_3C_2T_X$ MXene for Highly Efficient NO Electroreduction to NH_3, ACS Mater. Lett., 2024, 6 (5), 1711−1721.